

Journal of
Applied Remote Sensing



Three-dimensional FLASH laser radar range estimation via blind deconvolution

Jason R. McMahon
Richard K. Martin
Stephen C. Cain



Report Documentation Page			<i>Form Approved OMB No. 0704-0188</i>	
<p>Public reporting burden for the collection of information is estimated to average 1 hour per response, including the time for reviewing instructions, searching existing data sources, gathering and maintaining the data needed, and completing and reviewing the collection of information. Send comments regarding this burden estimate or any other aspect of this collection of information, including suggestions for reducing this burden, to Washington Headquarters Services, Directorate for Information Operations and Reports, 1215 Jefferson Davis Highway, Suite 1204, Arlington VA 22202-4302. Respondents should be aware that notwithstanding any other provision of law, no person shall be subject to a penalty for failing to comply with a collection of information if it does not display a currently valid OMB control number.</p>				
1. REPORT DATE OCT 2009	2. REPORT TYPE	3. DATES COVERED 00-00-2009 to 00-00-2009		
4. TITLE AND SUBTITLE Three-dimensional FLASH laser radar range estimation via blind deconvolution			5a. CONTRACT NUMBER	
			5b. GRANT NUMBER	
			5c. PROGRAM ELEMENT NUMBER	
6. AUTHOR(S)			5d. PROJECT NUMBER	
			5e. TASK NUMBER	
			5f. WORK UNIT NUMBER	
7. PERFORMING ORGANIZATION NAME(S) AND ADDRESS(ES) Air Force Institute of Technology, Graduate School of Engineering and Management, 2950 Hobson Way, Wright Patterson AFB, OH, 45433			8. PERFORMING ORGANIZATION REPORT NUMBER	
9. SPONSORING/MONITORING AGENCY NAME(S) AND ADDRESS(ES)			10. SPONSOR/MONITOR'S ACRONYM(S)	
			11. SPONSOR/MONITOR'S REPORT NUMBER(S)	
12. DISTRIBUTION/AVAILABILITY STATEMENT Approved for public release; distribution unlimited				
13. SUPPLEMENTARY NOTES				
14. ABSTRACT				
15. SUBJECT TERMS				
16. SECURITY CLASSIFICATION OF:			17. LIMITATION OF ABSTRACT Same as Report (SAR)	18. NUMBER OF PAGES 29
a. REPORT unclassified	b. ABSTRACT unclassified	c. THIS PAGE unclassified	19a. NAME OF RESPONSIBLE PERSON	

Three-dimensional FLASH laser radar range estimation via blind deconvolution

Jason R. McMahon, Richard K. Martin, and Stephen C. Cain

^aAir Force Institute of Technology, Graduate School of Engineering and Management, 2950 Hobson Way, Wright Patterson AFB, Ohio 45433, USA
jason.mcmahon@us.af.mil, richard.martin@afit.edu, and stephen.cain@afit.edu

Abstract. Three dimensional (3D) FLASH Laser Radar (LADAR) sensors are unique due to the ability to rapidly acquire a series of two dimensional remote scene data (i.e. range images). Principal causes of 3D FLASH LADAR range estimation error include spatial blur, detector blurring, noise, timing jitter, and inter-sample targets. Unlike previous research, this paper accounts for pixel coupling by defining the range image mathematical model as a 2D convolution between the system spatial impulse response and the object (target or remote scene) at a particular point in time. Using this model, improved range estimation is possible by object restoration from the data observations. Object estimation is performed by deriving a blind deconvolution Generalized Expectation Maximization (GEM) algorithm with the range determined from the estimated object by a normalized correlation method. Theoretical derivations and simulation results are verified with experimental data of a bar target taken from a 3D FLASH LADAR system in a laboratory environment. Simulation examples show that the GEM improves range estimation over the unprocessed data and a Wiener filter method by 75% and 26% respectively. In the laboratory experiment, the GEM improves range estimation by 34% and 18% over the unprocessed data and Wiener filter method respectively.

Keywords: 3D FLASH LADAR, laser radar, range estimation, blind deconvolution, object restoration, waveform processing, generalized expectation maximization

1 INTRODUCTION

A three-dimensional (3D) FLASH laser radar (LADAR) is a pulsed radar system this is both an imaging and ranging sensor. Referring to Fig. 1, a 3D FLASH LADAR produces a time sequence of two-dimensional (2D) images due to a fast range gate resulting in a 3D data cube of spatial and range scene data with excellent range resolution [1], [2]. FLASH technology principally differs from scanning LADAR by being able to form a 3D representation of a remote scene in one laser pulse rather than rastering a 3D scene together using many pulses. This capability results in faster scene collection times with lighter weight, lower power, and reduced mechanical complexity as compared to the scanning systems. Practical applications of 3D FLASH LADAR include intelligence, surveillance, and reconnaissance (ISR), rendezvous and capture (air and space), collision avoidance (COLA) for manned and unmanned air/ground vehicles, and weapon targeting.

Typically, a 3D FLASH LADAR operates in one of two modes. The first mode is called “HIT mode” where each pixel element (pixel) is independently triggered when its intensity reaches a preset threshold. This mode is advantageous when searching for a target where the range is not already known. However, truncated waveforms can occur leading to range estimation errors. The second mode is called “SULAR mode” where the pixels are triggered to start recording data together based on a preset range. Benefits of this mode include being able to successively capture fine details of the target and background. Drawbacks are that the target range must be known a priori and waveforms are truncated for targets near the end of the collect.

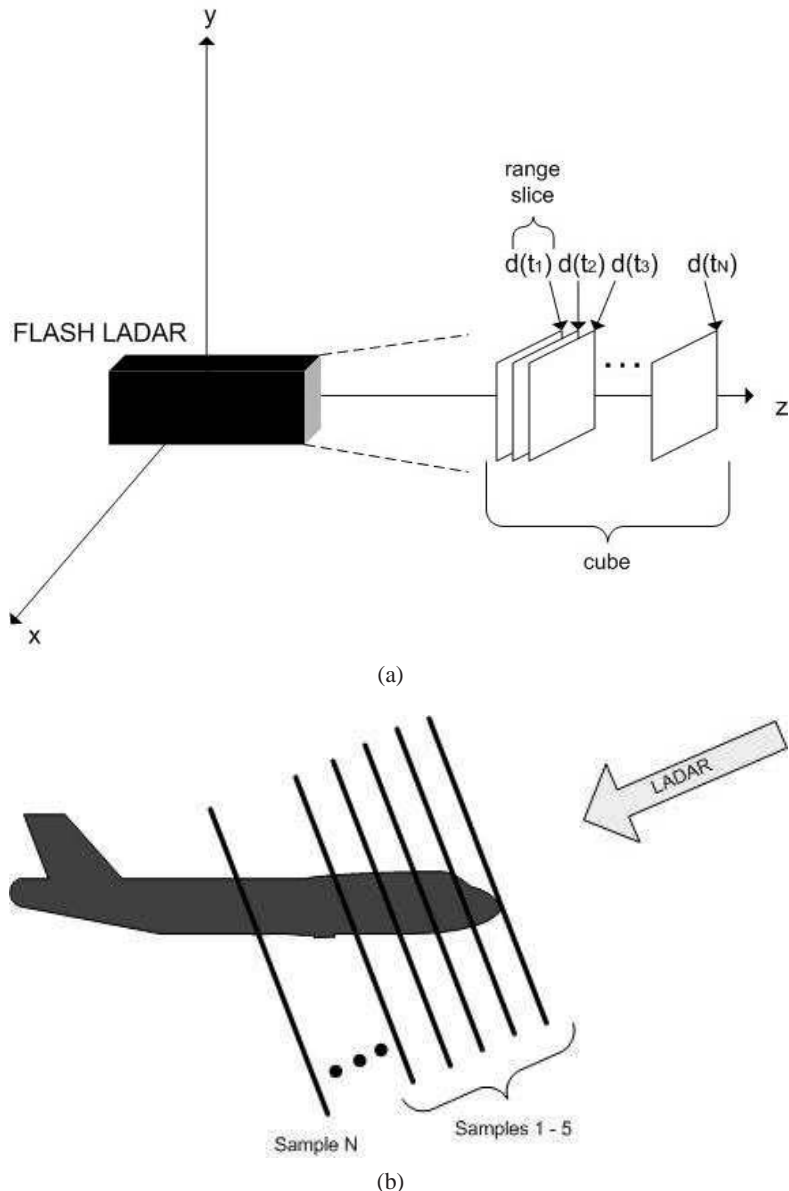


Fig. 1. (a) 3D view of LADAR system model in Cartesian coordinates with each data cube having dimensions of pixel \times pixel \times time sample. The variable $d(t_k)$ corresponds to the k^{th} receiver detected range image with $k \in [1, N]$. (b) Another view of the 3D FLASH LADAR operation. Each range image's full field of view (FOV) is 128×128 pixels with a range gate near 2 nanoseconds corresponding to the 3D FLASH LADAR system used for experimental collects.

A method to model the 3D FLASH LADAR data operating in SULAR mode is that the 2D range images are formed via a convolution between the object at a particular time and the spatial impulse response. In Fig. 1(a), a range image $d(t_k)$ is one of the 2D slices of the data cube. Considering the laser illuminating a target, one collects from a 3D FLASH LADAR sensor results in a data cube consisting of a series of range images (N from Fig. 1) representing detected photons.

Attempts at 3D FLASH LADAR range estimation of a remote scene can result in errors due to several factors including the optical spatial impulse response, detector blurring, photon noise, timing jitter, and readout noise. These factors either cause the scene's intensity to spread across pixels or add unwanted and disruptive noise effects. The intensity spreading and noise corrupts the correct pixel intensities by mixing intensities with neighboring pixels thereby providing false intensity values and therefore incorrect photon counts to the range estimator. Without blur and noise compensation, the range estimates would be inaccurate to a degree depending on the blur and noise severity.

The *motivation* behind this paper is to provide a means of improving range estimation by object recovery (i.e. spatially deblurring data) from 3D FLASH LADAR observations. Referring to Fig. 1(a), the idea is to process the data in the spatial dimensions (x, y) while improving ranging performance in the time dimension (z).

The theoretical development of the range estimator algorithm is covered first and then verified using simulation and experimental results. The algorithm is a variation on the Expectation Maximization (EM) algorithm called Generalized Expectation Maximization (GEM) and is desirable due to its iterative likelihood maximization, convergence properties, and ability to decouple terms [3]. The GEM algorithm is powerful in that it can perform blind deconvolution in situations with severe defocus or other aberrations including atmospheric turbulence. To account for different scenarios, two versions of the GEM algorithm are derived that either recover the *pulse-shape* or the *object*. The primary difference between the two involves data required and accuracy. *Pulse-shape* estimation requires less data, but is less accurate than *object* estimation. Additional details of the differences are presented in Sections 2.3 and 2.4.

In addition to the GEM algorithms, a Wiener filter method is used to attempt range estimation improvement via object recovery from 3D FLASH LADAR observations [4], [5]. Requiring spatial impulse response knowledge *a priori*, this method can only perform deconvolution unlike the blind deconvolution ability of the GEM. The purpose for adding this other method is to show that the GEM outperforms a competing algorithm that already knows part of the answer (spatial impulse response).

2 THEORETICAL

This section discusses incoherent imaging and the application to 3D FLASH LADAR, presents the data model, and develops the GEM algorithms that perform object recovery leading to improved range estimation. Even though the laser light is partially coherent, the argument is made that the detected light is able to be modeled as fully incoherent. Consequently, this allows for the returns to be a result of a linear, spatially invariant (LSI) system involving an intensity convolution (instead of amplitude convolution) between the intensity point spread function and the remote scene. Linearity is a consequence of electromagnetic wave propagation theory, and spatial invariance results from remaining with the isoplanatic angle [6]. Utilizing this LSI convolution model, two GEM blind deconvolution algorithms are developed that enable improved range estimation.

2.1 Incoherent imaging

Both the negative binomial and Poisson distributions can be used to capture the non-negative, discrete nature of the laser light. The negative binomial distribution would be the most optimal

in describing the illuminating partially coherent laser light, but blind deconvolution methods are cumbersome [7]. Whereas, blind deconvolution methods with the Poisson distribution (incoherent imaging) are more tractable and, thus, utilized in this research. Even if the speckle is severe, the benefit of modeling the speckle does not outweigh the cost of implementing a partially coherent blind deconvolution model for the 3D FLASH LADAR system. Previous research using the incoherent data model for a 3D FLASH LADAR has also experienced success [8], [9].

To gain more insight into this assumption, a simple approach is to estimate the amount of coherence contained within the 3D FLASH LADAR data by estimating the speckle parameter of the negative binomial distribution directly from the data [7]. Capturing both temporal and spatial coherence, if the speckle parameter estimate is high enough, the negative binomial distribution will look Poisson-like allowing the data observations to be modeled as arising from an intensity convolution (incoherent imaging). Including speckle and photon noise effects, the negative binomial probability mass function (PMF) describes the photon distribution of a partially coherent imaging system for a single pixel or [7]

$$P(K) = \frac{\Gamma(K + \mathcal{M})}{\Gamma(K + 1)\Gamma(\mathcal{M})} \left[1 + \frac{\mathcal{M}}{K}\right]^{-K} \left[1 + \frac{\bar{K}}{\mathcal{M}}\right]^{-\mathcal{M}} \quad (1)$$

where \mathcal{M} is the speckle parameter and \bar{K} is the pixel's average photon count. Changing the distribution for a 3D FLASH LADAR, the illuminating laser light statistics for a particular volume element (voxel) (x, y, k remain constant) across many data cubes is

$$P(D_{jk}(x, y) = d_{jk}(x, y) \forall j \in (1, 2, \dots, J)) = \prod_{j=1}^J \frac{\Gamma(d_{jk}(x, y) + \mathcal{M})}{\Gamma(d_{jk}(x, y) + 1)\Gamma(\mathcal{M})} \left[1 + \frac{\mathcal{M}}{K}\right]^{-d_{jk}(x, y)} \left[1 + \frac{\bar{K}}{\mathcal{M}}\right]^{-\mathcal{M}} \quad (2)$$

where j represents the data cubes, k is the range image (i.e. time variable) within a data cube, (x, y) are the coordinates in the image plane, and $d_{jk}(x, y)$ is the data observation. The voxels are assumed statistically independent from each other because of the discrete nature of photons and the detected photons do not affect future detected photons. The maximum likelihood solution for the average voxel intensity is determined by

$$\bar{K} = \frac{1}{J} \sum_{j=1}^J d_{jk}(x, y). \quad (3)$$

Taking the natural log of Equation (2) yields

$$\ln [P(D_{jk}(x, y) = d_{jk}(x, y) \forall j \in (1, 2, \dots, J))] = \sum_{j=1}^J \ln \left[\frac{\Gamma(d_{jk}(x, y) + \mathcal{M})}{\Gamma(d_{jk}(x, y) + 1)\Gamma(\mathcal{M})} \right] - d_{jk}(x, y) \ln \left[1 + \frac{\mathcal{M}}{K} \right] - \mathcal{M} \ln \left[1 + \frac{\bar{K}}{\mathcal{M}} \right] \quad (4)$$

where graphical methods are employed to find the speckle parameter that maximizes this log-likelihood. Using the same experimental data as in the range estimation efforts, a collection of voxels with the strongest laser light are chosen to estimate the speckle parameter. Figure 2 shows the similarities between the negative binomial and Poisson distribution using an average of the estimated speckle parameter.

Even without considering speckle parameter estimation results, the argument can be made for incoherent imaging due to the Poisson distribution's ability to model the non-negativity and discrete nature of light [8], [9]. This argument is solidified by the speckle parameter estimation results indicating that the speckle noise appears low enough for the incoherent imaging model to be used with confidence.

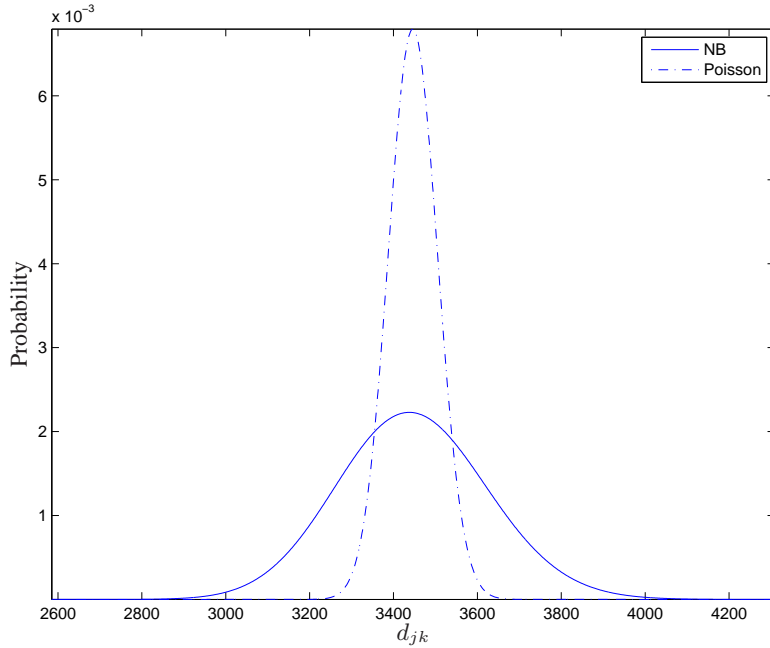


Fig. 2. This plot shows the negative binomial (NB) using an estimated average speckle parameter versus the Poisson distribution with the same mean. While not identical, the negative binomial distribution compares well enough to the Poisson distribution to assume incoherent imaging.

2.2 Data model

Considering a 3D FLASH LADAR sensor with statistically independent samples, the PMF of the observed photons, $d_{jk}(x, y)$, incorporating all cubes ($j \in [1, J]$), range samples ($k \in [1, K]$), and detector pixels ($x \in [1, X], y \in [1, Y]$) is

$$P[D_{jk}(x, y) = d_{jk}(x, y); \forall j, k, x, y] = \prod_{j, k, x, y} \frac{[i_{jk}(x, y) + B(x, y)]^{d_{jk}(x, y)} \exp\{-[i_{jk}(x, y) + B(x, y)]\}}{d_{jk}(x, y)!} \quad (5)$$

where the data observations are defined by

$$d_{jk}(x, y) = i_{jk}(x, y) + B(x, y) + n_{jk}(x, y) \quad (6)$$

with $i_{jk}(x, y)$ as the blurry, non-noisy data, $B(x, y)$ as the pixel bias, and $n_{jk}(x, y)$ as a general noise term accounting for all noise sources (i.e. photon noise, thermal noise, readout noise, etc.). The (x, y) and k variables correspond to a pixel in the detector array and to the returned signal time of arrival respectively. The time of arrival is computed based on the time from laser pulse transmission to photon detection. The blurry, non-noisy data is

$$i_{jk}(x, y) = \sum_{m=1}^M \sum_{n=1}^N o_k(m, n) h_j(x - m, y - n) \quad (7)$$

where the object $o_k(m, n)$ is defined at the object plane with coordinates ($m \in [1, M], n \in [1, N]$) and changes within a single cube, but is considered constant across all cubes. This assumption requires the ability to perform cube registration due to the possibility of moving targets, moving sensor platform, or inter-cube timing errors. Incorporating contributions from

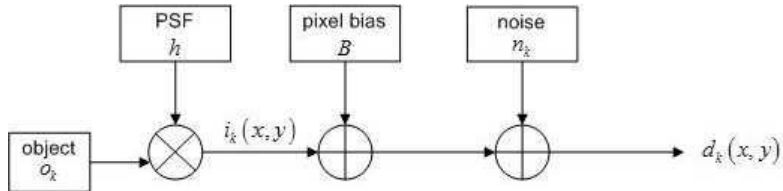


Fig. 3. 3D FLASH LADAR data block diagram. For an arbitrary cube (j notation ignored), the observed data is an addition \oplus of the pixel bias, the noise, and the blurry, non-noisy image (convolution, depicted by \otimes , between object and PSF).

light propagation, optical aberrations, and atmospheric blurring, the intensity point spread function (PSF) $h_j(x, y)$ is constant within a single cube while changing across cubes. In this research, the PSF is considered constant within a single cube since collection times spans under forty nanoseconds and any time-dependent effects would be essentially frozen. In addition, the pixel bias $B(x, y)$ is constant between cubes as well as within a single cube due to the pixel's unchanging physical material and response to incident light.

Every pixel in the detector array records a time-delayed and attenuated version of the transmitted pulse. The physical outgoing pulse shape of a 3D FLASH LADAR is either Gaussian, negative parabolic, or some hybrid of the two. The object can be defined by an amplitude term and a pulse shape or

$$o_k(m, n) = A(m, n) p_k(m, n). \quad (8)$$

Assuming a Gaussian transmitted pulse, the object is

$$o_k(m, n) = \frac{A(m, n)}{\sqrt{2\pi}\sigma_w} \exp \left\{ \frac{-(t_k - 2R(m, n)/c)^2}{2\sigma_w^2} \right\} \quad (9)$$

where $A(m, n)$ is the object amplitude, σ_w is the waveform standard deviation, t_k is the time variable, c is the speed of light, and $R(m, n)$ is the range to the target. For military targeting or navigation, range to target (located in the object term) is the desired unknown variable. For a negative parabolic waveform shape, the object is defined by

$$o_k(m, n) = A(m, n) \left[1 - \frac{(2R(m, n) - t_k c)^2}{(cp_w)^2} \right] \text{rect} \left(\frac{2R(m, n) - t_k c}{2cp_w} \right) \quad (10)$$

where $2p_w$ is the pulse width and rect is the rectangle function defined by

$$\text{rect}(x) = \begin{cases} 0, & \text{if } |x| > 1/2 \\ 1/2, & \text{if } |x| = 1/2 \\ 1, & \text{if } |x| < 1/2. \end{cases} \quad (11)$$

In attempting to perform range estimation, a range term is not explicitly in the model, but it is buried within the object, $o_k(m, n)$, term given by Equations (9) and (10). If the object were known, the target range could be then extracted from the object by peak detection methods. Therefore, the goal in this paper is to accurately estimate the object and recover the range by using a modified version of peak detection that permits sub-sample ranging. Sub-sample ranging is done to account for targets that are between adjacent recorded samples.

The unknown parameters in this estimation scenario are the object (target amplitude and target range), PSF, and pixel bias. The variable of interest in this paper is the range term residing in Equation (9) or (10). Direct estimation of the range term is problematic because of its location either in an exponential or in a squared term. Therefore, the approach to range estimation is to retrieve the range from the estimated pulse-shape or object. This methodology relies

on the knowledge that the target produces the waveform peak in the detected returns. Concerning the PSF, blind deconvolution techniques must be employed since the PSF is unknown. Blind deconvolution has a rich heritage in astronomical imaging providing a bevy of literature attempting blind deconvolution. Although, blind deconvolution in astronomical cases consists of trying to recover one object and one PSF (or many PSFs if using multiple frames). In trying to recover the target range from one 3D FLASH LADAR data collect, this problem consists of many objects with one PSF. There are many objects due to the transmitted waveform causing each range slice to contain different intensities corresponding to where the waveform is incident on the object. Therefore, these incident points become distinct objects in the blind deconvolution framework. If multiple cubes are necessary, the atmosphere is changing with each cube resulting in multiple PSFs that must be estimated resulting in a “multi-frame” or “multi-cube” scenario. If no atmospheric turbulence exists or is non-volatile, the PSF is consistent throughout the cubes and the j subscript can be dropped.

Traditional linear maximum likelihood efforts do not suffice to estimate target range given the unknowns in the statistical model depicted by Equation (5). More powerful object estimation methods like the EM algorithm must be employed due to the coupled unknowns which will be covered in the next section. However, a closed form solution for the EM algorithm’s maximization step is intractable. Consequently, the GEM algorithm goal is to modify the EM structure such that the likelihood is incrementally increased rather than globally maximized as in the EM algorithm. This incremental increase in the likelihood simplifies the maximization step allowing unknown, non-random parameter estimation. In summary, the GEM algorithm is written as

$$Q(\Psi^{(v+1)}; \Psi^{(v)}) \geq Q(\Psi^{(v)}; \Psi^{(v)}) \quad (12)$$

where Ψ is the vector of unknown variables, v is the iteration, and Q is the expected value of the complete data log-likelihood or

$$Q(\Psi; \Psi^{(v)}) = E_{\Psi^{(v)}} \{ \ln L_{CD}(\Psi|y) \} \quad (13)$$

with L_{CD} as the complete data likelihood and y as the incomplete data. Complete data can be viewed as the unobserved variables (fabricated or not) used to simplify the problem. Incomplete data is usually the observed data. If Equation (12) holds, it has been shown that the likelihood is increased with every iteration or [3]

$$L(\Psi^{(k+1)}) \geq L(\Psi^{(k)}) \quad (14)$$

and, if bounded, the GEM sequence converges to a local maximum due to the monotonicity of the algorithm.

With the target range extracted from the estimated object, object recovery is accomplished using two approaches concerning the pulse-shape and object variables from Equation (9). The pulse-shape estimation is very powerful in that the estimator only needs *one* data cube (one-shot, one-kill). However, if the best accuracy is required and the 3D data cubes are properly registered, the multi-cube object estimation provides lower error.

2.3 Range estimation using pulse-shape recovery via the GEM algorithm

Considering pulse-shape recovery with only one cube required for processing (ignoring j , since $j = 1$), the problem is reformed by calling the original data, $d_k(x, y)$, the incomplete data and specifying

$$d_k(x, y) = \sum_{m=1}^M \sum_{n=1}^N \tilde{d}_k(x, y|m, n) + \tilde{q}_k(x, y) \quad (15)$$

where two new variables, $\tilde{d}_k(x, y|m, n)$ and $\tilde{q}_k(x, y)$, are called complete data. This formulation provides two sets of complete data that account for the photon noise/image formation and pixel bias respectively. The formation of the complete data highlights the powerful nature of the EM algorithm. In this application, complete data can also be called unobserved data and carries no explicit physical meaning. It is used to directly benefit the EM algorithm. Consistent with [10], careful definition of the complete data allows decoupling of unknown variables while preserving physical meaning in the expected value of the incomplete data.

The expected value of the complete data sets is given by

$$E \left[\tilde{d}_k(x, y|m, n) \right] = A(m, n) p_k(m, n) h(x - m, y - n). \quad (16)$$

and

$$E \left[\tilde{q}_k(x, y) \right] = B(x, y) \quad (17)$$

where $B(x, y)$ is the constant pixel bias. The expected value of the incomplete data is thus

$$E \left[d_k(x, y) \right] = i_k(x, y) + B(x, y) \quad (18)$$

which is consistent with the data observations depicted in Fig. 3. Adding the pixel bias to the model covers non-modeled noise effects and pixel-to-pixel impulse response variations. The pixel bias is assumed to be governed by the Poisson distribution due to the discrete random nature of dark current and electron noise. Physically, the pixel bias is added to the photons incident upon the detector and is part of the detected photon counts. The PMF for the photon noise is

$$P \left(\tilde{d}_k(x, y|m, n) \right) = \frac{[A(m, n) p_k(m, n) h(x - m, y - n)]^{\tilde{d}_k(x, y)} e^{-[A(m, n) p_k(m, n) h(x - m, y - n)]}}{\tilde{d}_k(x, y)!} \quad (19)$$

while the PMF for the pixel bias is

$$P \left(\tilde{q}_k(x, y) \right) = \frac{B(x, y)^{\tilde{q}_k(x, y)} e^{-B(x, y)}}{\tilde{q}_k(x, y)!}. \quad (20)$$

Assuming statistical independence between all the pixels and between the photon noise and pixel bias noise, the complete data log-likelihood function considering all random variables is

$$L_{CD}(p_k, A, h, B) = \ln \left[\prod_{k, x, y, m, n} P \left(\tilde{d}_k(x, y|m, n) \right) P \left(\tilde{q}_k(x, y) \right) \right] \quad (21)$$

or (NOTE: summations wrap around unless otherwise stated)

$$L_{CD}(p_k, A, h, B) = \sum_{k, x, y, m, n} \tilde{d}_k(x, y|m, n) \ln [A(m, n) p_k(m, n) h(x - m, y - n)] - [A(m, n) p_k(m, n) h(x - m, y - n)] + \tilde{q}_k(x, y) \ln [B(x, y)] - B(x, y). \quad (22)$$

Referring to Equation (13), the Q function then becomes

$$Q(p_k, A, h, B) = E \left[L_{CD}(p_k, A, h, B) | d_k(x, y), p_k^{old}, A^{old}, h^{old}, B^{old} \right] \quad (23)$$

where the estimates for the amplitude, pulse-shape, PSF, and bias are considered maximum-likelihood estimates. Taking the conditional expectation of Equation (23) results in

$$\begin{aligned} Q(p_k, A, h, B) = & \sum_{k,x,y,m,n} \mu_{\tilde{d}}^{old}(m, n; p_k^{old}, A^{old}, h^{old}) \ln [A(m, n) p_k(m, n) h(x - m, y - n)] \\ & - [A(m, n) p_k(m, n) h(x - m, y - n)] + \mu_{\tilde{q}}^{old}(x, y; B^{old}) \ln [B(x, y)] \\ & - B(x, y) \end{aligned} \quad (24)$$

where

$$\mu_{\tilde{d}}^{old}(m, n; p_k^{old}, A^{old}, h^{old}) = E \left[\tilde{d}_k(x, y | m, n) | d_k(x, y), p_k^{old}, A^{old}, h^{old} \right] \quad (25)$$

and

$$\mu_{\tilde{q}}^{old}(x, y; B^{old}) = E \left[\tilde{q}_k(x, y) | d_k(x, y), B^{old} \right]. \quad (26)$$

Equations (25) and (26) represent the expected value of one set of complete data given the incomplete data. For Poisson random variables, these expectations turn out to be ratio of the data times one expected value of the complete data divided by the all sets of expected values of the complete data [11]. For the first set of complete data, $\tilde{d}_k(x, y)$, the conditional expectation is

$$\mu_{\tilde{d}}^{old}(m, n; p_k^{old}, A^{old}, h^{old}) = \frac{d_k(x, y) A^{old}(m, n) p_k^{old}(m, n) h^{old}(x - m, y - n)}{i_k^{old}(x, y) + B^{old}(x, y)}. \quad (27)$$

while the second set of complete data concerning the pixel bias $\tilde{q}_k(x, y)$, has a conditional expectation equal to

$$\mu_{\tilde{q}}^{old}(x, y; B^{old}) = \frac{d_k(x, y) B^{old}(x, y)}{i_k^{old}(x, y) + B^{old}(x, y)}. \quad (28)$$

The maximization of the Q function for all parameter unknowns (target amplitude, target pulse shape, PSF, and pixel bias) is theoretically intractable due to coupling. It is required to break apart the Q function into separate components such that

$$Q = Q_p + Q_h + Q_A + Q_B \quad (29)$$

where each component of the Q function can be maximized independently. Thus, the GEM algorithm becomes

$$\begin{aligned} Q_p(p_k^{new} | p_k^{old}, A^{old}, h^{old}) & \geq Q_p(p_k^{old} | p_k^{old}, A^{old}, h^{old}) \\ Q_A(A^{new} | p_k^{old}, A^{old}, h^{old}) & \geq Q_A(A^{old} | p_k^{old}, A^{old}, h^{old}) \\ Q_h(h^{new} | p_k^{old}, A^{old}, h^{old}) & \geq Q_h(h^{old} | p_k^{old}, A^{old}, h^{old}) \\ Q_B(B^{new} | B^{old}) & \geq Q_B(B^{old} | B^{old}) \end{aligned} \quad (30)$$

which, if these conditions are met, ensures that the likelihood is increased with each iteration [3]

$$L(p_k^{new}, A^{new}, h^{new}, B^{new}) \geq L(p_k^{old}, A^{old}, h^{old}, B^{old}) \quad (31)$$

resulting in a GEM sequence converging to a local minimum.

Beginning the estimation process of the separate Q functions starts with the target pulse shape, Q_p which is

$$Q_p = \sum_{k,x,y,m,n} \mu_d^{old} (m, n; p_k^{old}, A^{old}, h^{old}) \ln [p_k (m, n)] - \lambda (m, n) \left[\sum_{k=1}^K p_k (m, n) - 1 \right] \quad (32)$$

where a pixel-dependent Lagrange multiplier, $\lambda (m, n)$, is introduced to force the pulse shape to add to one for each pixel. This constraint is necessary to decouple the pulse shape from the target amplitude and PSF. Taking the derivative of Equation (32) with respect to a particular object plane point and range sample, setting the result equal to zero, $\partial Q_p / \partial p_{k_o} (m_o, n_o) = 0$, and solving for the pulse shape, results in

$$p_{k_o}^{new} (m_o, n_o) = p_{k_o}^{old} (m_o, n_o) \left(\frac{A^{old} (m_o, n_o)}{\lambda (m_o, n_o)} \right) \sum_{x=1}^X \sum_{y=1}^Y \frac{d_{k_o} (x, y) h^{old} (x - m_o, y - n_o)}{i_{k_o}^{old} (x, y) + B^{old} (x, y)} \quad (33)$$

where

$$\lambda (m_o, n_o) = A^{old} (m_o, n_o) \sum_{k=1}^K p_k^{old} (m_o, n_o) \sum_{x=1}^X \sum_{y=1}^Y \frac{d_k (x, y) h^{old} (x - m_o, y - n_o)}{i_k^{old} (x, y) + B^{old} (x, y)} \quad (34)$$

and

$$i_{k_o}^{old} (x, y) = \sum_{m=1}^M \sum_{n=1}^N A^{old} (m, n) p_{k_o}^{old} (m, n) h^{old} (x - m, y - n). \quad (35)$$

Equation (33) is the iterative solution for the pulse shape per range sample. Next, the Q function is partitioned into its target amplitude components

$$Q_A = \sum_{k,x,y,m,n} \{ \mu_{\tilde{d}}^{old} (m, n; p_k^{old}, A^{old}, h^{old}) \ln [A (m, n)] \} - \sum_{m=1}^M \sum_{n=1}^N A (m, n) \quad (36)$$

where

$$\sum_{x=1}^X \sum_{y=1}^Y h (x, y) = 1 \quad (37)$$

$$\sum_{k=1}^K p_k (m, n) = 1 \quad (38)$$

have been utilized to decouple the pulse shape and PSF terms from the target amplitude. Maximizing Equation (36) by $\partial Q_A / \partial A (m_o, n_o) = 0$ and solving for the amplitude term results in the iterative solution for the target amplitude term

$$A^{new} (m_o, n_o) = A^{old} (m_o, n_o) \sum_{k=1}^K p_k^{old} (m_o, n_o) \sum_{x=1}^X \sum_{y=1}^Y \frac{d_k (x, y) h^{old} (x - m_o, y - n_o)}{i_k^{old} (x, y) + B^{old} (x, y)}. \quad (39)$$

The PSF is the final unknown parameter that uses the first set of complete data, $\tilde{d}_k (x, y)$. The Q function for the PSF is

$$Q_h = \sum_{k,x,y,m,n} \mu_{\tilde{d}}^{old} (m, n; p_k^{old}, A^{old}, h^{old}) \ln [h (x - m, y - n)] - [A (m, n) p_k (m, n) h (x - m, y - n)], \quad (40)$$

which still has the target amplitude and pulse shape terms. Similar to [10], a change of variables is required to remove the dependence on the pulse shape and to allow for easier differentiation. Utilizing $\sum_{k=1}^K p_k(m, n) = 1$ and setting $m' = x - m$ and $n' = y - n$, Q_h then becomes

$$Q_h = \sum_{k,x,y,m',n'} \left\{ \mu_d^{old}(x - m', y - n'; p_k^{old}, A^{old}, h^{old}) \ln[h(m', n')] \right\} - \sum_{x,y,m',n'} A(x - m', y - n') h(m', n'). \quad (41)$$

Setting $\partial Q_h / \partial h(m'_o, n'_o) = 0$ and solving for the PSF produces the iterative solution

$$h^{new}(m'_o, n'_o) = h^{old}(m'_o, n'_o) \sum_{k,x,y} \frac{d_k(x, y) A(x - m'_o, y - n'_o) p_k^{old}(x - m'_o, y - n'_o)}{(i_k^{old}(x, y) + B^{old}(x, y)) \sum_{x=1}^X \sum_{y=1}^Y A(x - m'_o, y - n'_o)}. \quad (42)$$

Usually, the target amplitude term in the denominator would be an issue because it is considered the new estimate. However, Equation (39) is the new estimate and can replace the target amplitude in the denominator resulting in a consistent solution for the PSF. Finally, the pixel bias must be estimated. In order to estimate the pixel bias, the second set of complete data, $\tilde{q}_k(x, y)$, is utilized. The Q function for the pixel bias is

$$Q_B = \sum_{k=1}^K \sum_{x=1}^X \sum_{y=1}^Y \frac{d_k(x, y) B^{old}(x, y)}{i_k^{old}(x, y) + B^{old}(x, y)} \ln(B(x, y)) - B(x, y). \quad (43)$$

Setting $\partial Q_B / \partial B(x_o, y_o) = 0$ and solving for the pixel bias results in an iterative solution

$$B^{new}(x_o, y_o) = B^{old}(x_o, y_o) \sum_{k=1}^K \frac{d_k(x_o, y_o)}{(i_k^{old}(x_o, y_o) + B^{old}(x_o, y_o))} \quad (44)$$

corresponding to the pixel bias solution.

After a pre-determined number of iterations on Equations (33), (39), (42), and (44), range estimate updates for each pixel are generated by using a normalized correlation method between a reference waveform at sub-sample ranges and the GEM estimate for the pulse shape, p_k^{new} . The range-dependent reference waveform that results in the highest correlation is chosen and the corresponding range is the new range estimate for that pixel. The new range estimate is fed back into the pulse-shape to generate a new p_k^{old} followed by another set of GEM iterations. The process (GEM iterations followed by range updates) repeats with the new range estimates used in calculating p_k^{old} using Equation (33) and ceases when the mean square error (MSE) between the data and non-noisy range images reaches the stopping criteria. All previous amplitude, PSF, and pixel bias estimates carry over from one range update to the next. More specifically, iterations cease when the MSE is lower than the average data variance or

$$\sum_{k=1}^K \sum_{x=1}^X \sum_{y=1}^Y (d_{jk}(x, y) - I_k^{est}(x, y) - B^{new}(x, y))^2 < \sum_{k=1}^K \sum_{x=1}^X \sum_{y=1}^Y V_k(x, y) \quad (45)$$

with

$$I_k^{est}(x, y) = \sum_{m=1}^M \sum_{n=1}^N A^{new}(m, n) p_k^{new}(m, n) h^{new}(x - m, y - n) \quad (46)$$

and

$$V_k(x, y) = \sum_{j=1}^J \left(d_{jk}(x, y) - \frac{\sum_{j_2=1}^J d_{j_2 k}(x, y)}{J} \right)^2 \quad (47)$$

where the extents of j_2 are the same as j and V_k is an average variance for the volume elements (voxels) across many data cubes. In the experimental data, a specific distribution for the variance is not chosen in order to account for all noise sources. For the simulation data, the data variance is replaced by the average variance of the Poisson distribution due to it being a known and controlled noise source.

Once the GEM estimates the pulse-shape, the range for each pixel must be extracted. If simple peak detection is used, targets between the samples would have the wrong range estimate. In order to mitigate inter-sample targets, scaling, and waveform truncation issues, sub-sample ranging is performed on the pulse-shape by using a normalized correlation method based on the Pearson product-moment correlation coefficient. Using this coefficient forces each pixel's waveform to be zero mean and unit standard deviation. The normalized cross-correlation method is constructed as follows: The range vector of samples within a cube $R(t)$ is represented by

$$R(t) = \sum_{t=0}^{K-1} (z_{\min} + z_{\text{inc}}(t)) \quad (48)$$

where K is total number of samples, z_{\min} is the range of the first sample, and z_{inc} is the range increment per sample. Another range vector, $K_r(t')$ is constructed with the same maximum and minimum extents as $R(t)$, but with a smaller range increment per sample or

$$K_r(t) = \sum_{t=0}^{K'-1} (z_{\min} + z_f(t)) \quad (49)$$

where K' is the number of samples in K_r and z_f is the range increment. Since the extents of K_r match $R(p)$, $K' > K$ and $z_f < z_{\text{inc}}$. A 2D reference Gaussian waveform matrix is used with the K_r vector as the reference target location or

$$r_k(p) = \exp \left\{ \frac{-(t_k - 2K_r(p)/c)^2}{2\sigma_w^2} \right\} \quad (50)$$

where t_k is the time vector and $k \in [1, K]$. The zero mean and unit variance version of r_k is

$$S_2(p) = \frac{r_k(p) - \bar{r}_k(p)}{\sigma_r^2(p)} \quad (51)$$

where σ_r^2 and \bar{r}_k are the variance and average of r_k in the time dimension. Considering the range estimate for the $(m, n)^{\text{th}}$ pixel, the zero mean and unit variance version of the estimated pulse-shape, $p_k(m, n)$ is

$$S_1(m, n) = \frac{p_k(m, n) - \frac{\sum_{k=1}^K p_k(m, n)}{K'}}{\sigma_p^2(m, n)} \quad (52)$$

where σ_p^2 is the variance of $p_k(m, n)$ in the time dimension. With S_1 and S_2 determined, the normalized cross correlation denoted by \star is performed by

$$C_{K_r}(p) = \frac{S_2 \star S_1}{K'} \quad (53)$$

and finding the range estimate is accomplished by peak detection on C_{K_r} or

$$\hat{R} (m, n) = \arg \max_{z_f(p)} C_{K_r} (p) \quad (54)$$

In summary, the pulse-shape estimation algorithm steps are:

1. Initialize PSF, amplitude, and pixel bias
2. Determine initial ranges and input into pulse-shape
3. Perform GEM iterations using Equations (33), (39), (42), and (44)
4. Use normalized cross-correlation to find new range estimates with Equation (54)
5. Generate new pulse-shapes based on new ranges
6. Determine MSE and compare to stopping criteria
7. Repeat Steps 3 through 6 until stopping criteria violated
8. Range estimates taken from last execution of Step 4

2.4 Range estimation using object recovery via the GEM algorithm

When multiple cubes are available and properly registered spatially and temporally, another method to perform range estimation is to relax the constraint on the pulse-shape and assume just an object in the data model. This change mitigates the issue in the hardware data where the pulse-shape is vaguely known. Therefore, estimation is performed on o_k rather than on p_k from Equation (8). The problem setup is similar to the pulse-shape estimation (now with more than one cube) by calling the original data, $d_{jk}(x, y)$, the incomplete data and specifying

$$d_{jk} (x, y) = \sum_{m=1}^M \sum_{n=1}^N \tilde{d}_{jk} (x, y|m, n) + \tilde{q}_{jk} (x, y) \quad (55)$$

where two new variables, $\tilde{d}_{jk}(x, y|m, n)$ and $\tilde{q}_{jk}(x, y)$, are defined and called complete data. This formulation provides two sets of complete data that account for the image formation and pixel bias respectively. The same PSF can be assumed for adjacent collections due to a typical data collection scenario where environments shouldn't be changing rapidly (ignore j). Thus, the expected values of the complete data sets are given by

$$E \left[\tilde{d}_{jk} (x, y|m, n) \right] = o_k (m, n) h (x - m, y - n) \quad (56)$$

and

$$E \left[\tilde{q}_{jk} (x, y) \right] = B (x, y) \quad (57)$$

where $B(x, y)$ is the constant pixel bias. The expected value of the incomplete data is thus

$$E [d_{jk} (x, y)] = i_k (x, y) + B (x, y) . \quad (58)$$

The PMF for the photon noise is

$$P \left(\tilde{d}_k (x, y|m, n) \right) = \frac{[o_k (m, n) h (x - m, y - n)]^{\tilde{d}_{jk}(x, y|m, n)} \exp \{-o_k (m, n) h (x - m, y - n)\}}{\tilde{d}_{jk} (x, y|m, n)!} \quad (59)$$

while the pixel bias PMF is

$$P(\tilde{q}_{jk}(x, y)) = \frac{B(x, y)^{\tilde{q}_{jk}(x, y)} e^{-B(x, y)}}{\tilde{q}_{jk}(x, y)!}. \quad (60)$$

Assuming statistical independence between all the pixels and between the photon noise and pixel bias noise, the complete data log-likelihood is then

$$L_{CD}(o_k, h, B) = \ln \left[\prod_{j,k,x,y,m,n} P(\tilde{d}_{jk}(x, y|m, n)) P(\tilde{q}_{jk}(x, y)) \right] \quad (61)$$

or

$$L_{CD}(o_k, h, B) = \sum_{j,k,x,y,m,n} \tilde{d}_{jk}(x, y|m, n) \ln [o_k(m, n) h(x - m, y - n)] - [o_k(m, n) h(x - m, y - n)] + \tilde{q}_{jk}(x, y) \ln [B(x, y)] - B(x, y). \quad (62)$$

Referring to [3], the Q function becomes the expected value of the complete data log-likelihood function with respect to the incomplete data and old parameter estimates

$$Q(o_k, h, B) = E[L_{CD}(o_k, h, B) | d_{jk}(x, y), o_k^{old}, h^{old}, B^{old}]. \quad (63)$$

Taking the conditional expectation from Equation (63) results in

$$Q(o_k, h, B) = \sum_{j,k,x,y,m,n} \mu_{\tilde{d}}^{old}(m, n; o_k^{old}, h^{old}) \ln [o_k(m, n) h(x - m, y - n)] - [o_k(m, n) h(x - m, y - n)] + \mu_{\tilde{q}}^{old}(x, y; B^{old}) \ln [B(x, y)] - B(x, y) \quad (64)$$

where

$$\begin{aligned} \mu_{\tilde{d}}^{old}(m, n; o_k^{old}, h^{old}) &= E[\tilde{d}_{jk}(x, y|m, n) | d_{jk}(x, y), o_k^{old}, h^{old}] \\ &= \frac{d_{jk}(x, y) o_k^{old}(m, n) h^{old}(x - m, y - n)}{i_k^{old}(x, y) + B^{old}(x, y)} \end{aligned} \quad (65)$$

and

$$\begin{aligned} \mu_{\tilde{q}}^{old}(x, y; B^{old}) &= E[\tilde{q}_{jk}(x, y) | d_{jk}(x, y), B^{old}] \\ &= \frac{d_{jk}(x, y) B^{old}(x, y)}{i_k^{old}(x, y) + B^{old}(x, y)}. \end{aligned} \quad (66)$$

Similar to the pulse-shape estimation, the maximization of the Q function for all parameter unknowns (object, PSF, and pixel bias) is theoretically intractable due to coupling. It is required to break apart the Q function into separate components such that

$$Q = Q_o + Q_h + Q_B \quad (67)$$

where each component of the Q function can be maximized independently. Thus, the GEM algorithm becomes

$$\begin{aligned} Q_o(o_k^{new} | o_k^{old}, h^{old}) &\geq Q_o(o_k^{old} | o_k^{old}, h^{old}) \\ Q_h(h^{new} | o_k^{old}, h^{old}) &\geq Q_h(h^{old} | o_k^{old}, h^{old}) \\ Q_B(B^{new} | B^{old}) &\geq Q_B(B^{old} | B^{old}) \end{aligned} \quad (68)$$

ensuring that the likelihood is increased with each iteration [3]

$$L(o_k^{new}, h^{new}, B^{new}) \geq L(o_k^{old}, h^{old}, B^{old}) \quad (69)$$

resulting in a GEM sequence converging to a local minimum. The procedure to find the maxima of the Q functions is the same as in pulse-shape estimation. First, the object solution is found by specifying

$$Q_o = \sum_{j,k,x,y,m,n} \mu_{\tilde{d}}^{old}(m, n; o_k^{old}, h^{old}) \ln [o_k(m, n)] - o_k(m, n) h(x - m, y - n). \quad (70)$$

In order to maximize Q_o , the derivative of Equation (70) with respect to a particular object plane point and range sample is set equal to zero, $\partial Q_p / \partial o_{k_o}(m_o, n_o) = 0$. Solving for the object results in

$$o_{k_o}^{new}(m_o, n_o) = \frac{o_{k_o}^{old}(m_o, n_o)}{J} \sum_{j=1}^J \sum_{x=1}^X \sum_{y=1}^Y \frac{d_{jk_o}(x, y) h^{old}(x - m_o, y - n_o)}{i_{k_o}^{old}(x, y) + B^{old}(x, y)} \quad (71)$$

with J as the number of cubes and utilizing

$$\sum_{x=1}^X \sum_{y=1}^Y h(x, y) = 1 \quad (72)$$

and where

$$i_k^{old}(x, y) = \sum_{m=1}^M \sum_{n=1}^N o_k^{old}(m, n) h^{old}(x - m, y - n). \quad (73)$$

Equation (71) is the iterative solution for the pulse shape per range sample. The PSF is the other unknown parameter that uses the first set of complete data, $\tilde{d}_{jk}(x, y)$. The Q function for the PSF is

$$Q_h = \sum_{j,k,x,y,m,n} \mu_{\tilde{d}}^{old}(m, n; o_k^{old}, h^{old}) \ln [h(x - m, y - n)] - o_k(m, n) h(x - m, y - n). \quad (74)$$

Similar to [10], a change of variables is required to remove the dependence on the pulse shape and to allow for easier differentiation. Setting $m' = x - m$ and $n' = y - n$, Q_h then becomes

$$Q_h = \sum_{j,k,x,y,m',n'} \mu_{\tilde{d}}^{old}(x - m', y - n'; o_k^{old}, h^{old}) \ln [h(m', n')] - o_k(x - m', y - n') h(m', n') \quad (75)$$

Setting $\partial Q_h / \partial h(m'_o, n'_o) = 0$ and solving for the PSF produces the solution

$$h^{new}(m'_o, n'_o) = \frac{h^{old}(m'_o, n'_o)}{J \left[\sum_{k,x,y} o_k(x - m'_o, y - n'_o) \right]} \sum_{j,k,x,y} \frac{d_{jk}(x, y) o_k^{old}(x - m'_o, y - n'_o)}{i_k^{old}(x, y) + B^{old}(x, y)} \quad (76)$$

The object term in the denominator is the new estimate from Equation (71). Since, there are phase aberrations across the aperture and the PSF needs to be constrained, phase retrieval is performed on Equation (76) by the Gerchberg-Saxton algorithm [12]. In the pulse-shape estimation, it was the object (i.e. pulse-shape) that was constrained making the phase retrieval unnecessary. Finally, the pixel bias must be estimated. In order to estimate the pixel bias, the second set of complete data, $\tilde{q}_k(x, y)$, is utilized. The Q function for the pixel bias is

$$Q_B = \sum_{k=1}^K \sum_{x=1}^X \sum_{y=1}^Y \frac{d_{jk}(x, y) B^{old}(x, y)}{i_k^{old}(x, y) + B^{old}(x, y)} \ln (B(x, y)) - B(x, y). \quad (77)$$

Table 1. 3D FLASH LADAR parameters

Parameter	Value
Detector Array	128×128
Aperture Diameter (D)	2 mm
Mean Wavelength	$1.55 \mu\text{m}$
Focal Length	0.30 m
Target Range	5.21 m
Transmit Energy	10 mJ
Pulse Standard Deviation (σ_w)	3 ns
Beam Divergence	0.009 radians
Detector Size	$10 \mu\text{m}$
Detector Spacing	$100 \mu\text{m}$
Detector Array Fill Factor	100%
Detector Bandwidth	$0.5 \mu\text{m}$
Target Reflectivity	10%
Detector Array Size	30×30 pixels
Solar Irradiance	10 Watts/m ² /μm
D/r_o Seeing Condition	1.43
Frame Rate	30 Hz
Time Samples (per collect)	20
Sample Period (within a collect)	1.876 ns

Setting $\partial Q_B / \partial B(x_o, y_o) = 0$ and solving for the pixel bias results in

$$B^{new}(x_o, y_o) = \frac{B^{old}(x_o, y_o)}{JK} \sum_{j=1}^J \sum_{k=1}^K \left(\frac{d_{jk}(x_o, y_o)}{i_k^{old}(x_o, y_o) + B^{old}(x_o, y_o)} \right). \quad (78)$$

GEM iterations continue and cease when the mean-square error (MSE) violates the stopping criteria. Once the stopping criteria is reached, range estimates are determined by using the normalized cross-correlation method on the object estimate as described in the previous section.

In summary, the object estimation steps are:

1. Initialize object, PSF, and pixel bias
2. Perform one GEM iteration using Equations (71), (76), and (78)
3. Determine MSE and compare to stopping criteria
4. Repeat Steps 2 and 3 until stopping criteria reached
5. Use normalized cross-correlation to find new range estimates with Equation (54)

3 SIMULATION

In order to verify the theory, a simulation scenario was developed whereby targets are interrogated by a 3D FLASH LADAR defined by the parameters from Table 1. The goal is to perform range estimation given the noisy, blurry data observations. Results show range estimation improvement by performing object recovery either via a Wiener filter method or GEM algorithms as outlined in Sections 2.3 and 2.4. Our previous research has taken the approach to use a Wiener filter on each individual range slice and then use a pixel-based ranging method on the resulting “deblurred” data cube [5]. Performance will illustrate that the GEM algorithms provide increased error performance over the Wiener filter while, at the same time, being more

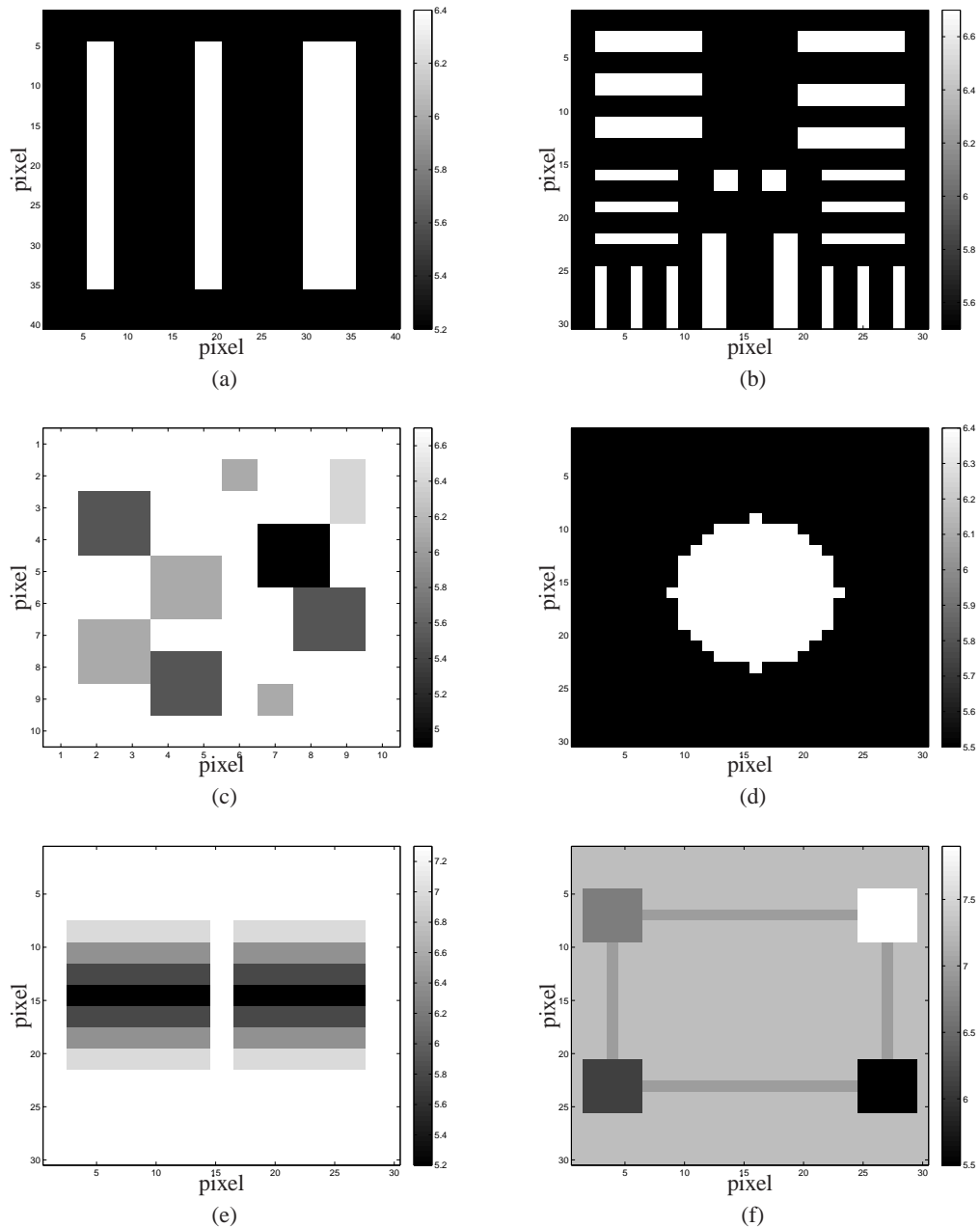


Fig. 4. True ranges for simulation targets: (a) three bars, (b) Many bars, (c) Various blocks, (d) Cylinder, (e) Slanted boards, and (f) Connected blocks. The target names in this caption correspond to the targets in Table 2. The three bar target is also the experimental data target. Other targets illustrate the robustness of the estimation algorithms.

Table 2. Range estimation results for simulation data

Data set	Metric	OD	WF	GEM _p	GEM _o
Three bars	RMSE (m)	0.402	0.346	0.163	0.100
	Corr	0.767	0.830	0.963	0.984
Many bars	RMSE (m)	0.596	0.561	0.346	0.365
	Corr	0.687	0.664	0.786	0.794
Slanted boards	RMSE (m)	0.225	0.171	0.161	0.131
	Corr	0.945	0.971	0.967	0.983
Cylinder	RMSE (m)	0.184	0.153	0.160	0.153
	Corr	0.877	0.925	0.945	0.962
Various blocks	RMSE (m)	0.473	0.209	0.344	0.175
	Corr	0.595	0.931	0.725	0.955
Connected blocks	RMSE (m)	0.208	0.133	0.158	0.112
	Corr	0.853	0.955	0.918	0.970

robust. Again, the GEM algorithms are more robust in that they do not need to know the point spread function, unlike the Wiener filter technique.

Using a Gaussian transmitted pulse, a 3D FLASH LADAR imaging scenario is developed in simulation using various geometrical shapes as targets shown in Fig. 4(a)-(f). One important clarification on the receiver optics is that the detector array has an effective fill factor of 100% by placing a micro-lens array in front of the pixels to focus the light onto the pixel. Also, the data includes effects from an average atmospheric turbulence to enable blind deconvolution. Range estimates are also determined without processing to enable further comparison between no processing and object recovery attempts. Results for all the targets and methods with error metrics are summarized in Table 2.

Table 2 clarifications: “RMSE” is root mean square error (RMSE) in meters between the true ranges and estimated ranges, “Corr” is an image quality metric referring to the correlation between the true range image and estimated range image signifying linear relationship strength (not to be confused with the normalized correlation ranging method), “OD” refers to the original data (OD) with no deblurring and ranges estimated by the normalized cross-correlation method, “WF” relates to range estimation using a Wiener Filter technique with normalized cross-correlation [5], “GEM_p” is the pulse-shape estimation GEM algorithm, and “GEM_o” is the object estimation GEM algorithm.

The targets of primary interest are the three bar target and the multiple bar target because the three bar target is also the experimental target and the multiple bar target is most sensitive to spatial blurring of all the targets. The bar targets are constructed in simulation consisting of two flat, perpendicular optically rough surfaces at different ranges. Referring to Figs. 4(a) and (b), the first surface in range has rectangular cut-out shapes while the second surface contains no cutouts. This type of target was chosen to highlight not only the coupling/blurring effects of the pixels along the edges of the rectangles, but also the decoupling and ranging capability of the GEM algorithm. The other targets are built in similar manner. Bar target shapes were used because the distances and shape dimensions can be physically measured in a laboratory environment to show range estimation improvement.

Table 2 and the range images from Figs. 4 and 5 show the negative effects of the blurring on range estimation juxtaposed with the positive effects from attempting recover the original object through Wiener filtering or the GEM algorithms. Implicit in the results is the ability to accurately estimate the pixel bias. Without it, the object model falls apart and range error becomes extremely large. Through simulation, the model and object recovery attempts have been verified. The final step is to use experimental data to validate simulation results.

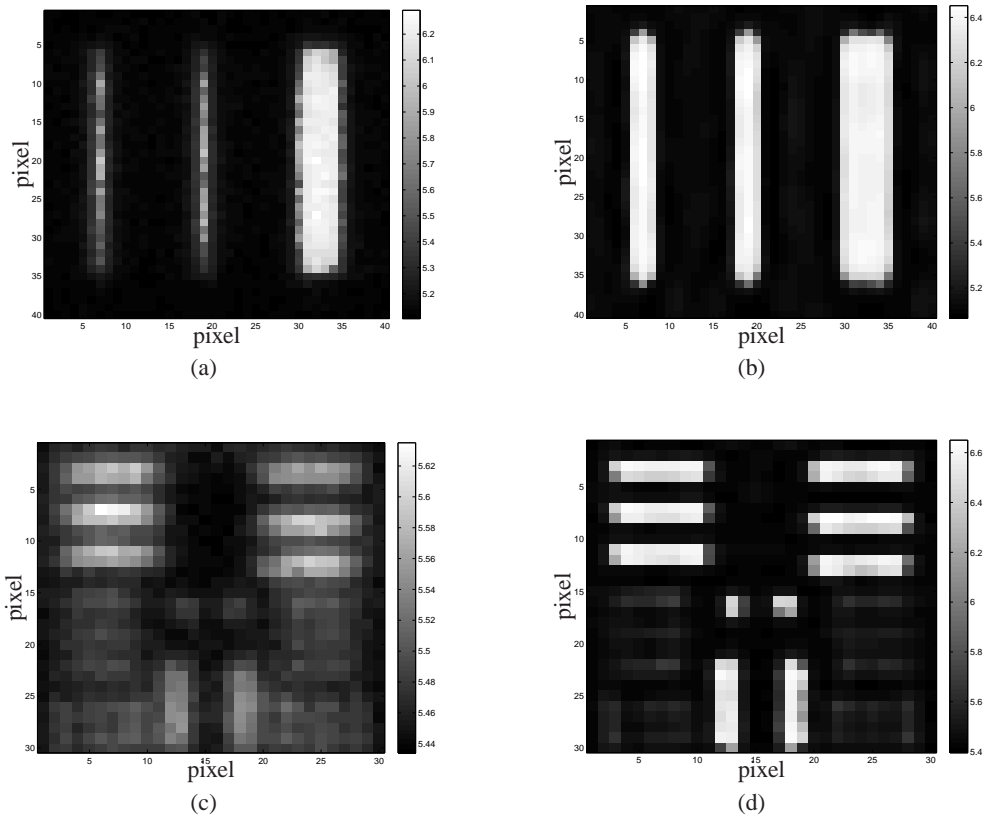


Fig. 5. Estimated ranges for simulation targets: (a) No processing - three bars, (b) GEM_o processing - three bars, (c) No processing - Many bars, and (d) GEM_o processing - Many bars. Utilizing the GEM_o algorithm, simulation results show the image quality improvement and improved range estimation (RMSE improves 75% for 3 bar target).

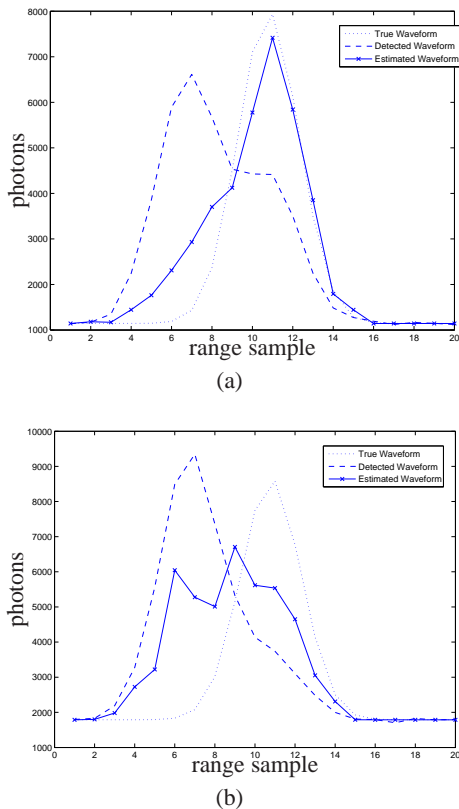


Fig. 6. (a) Using the data from Fig. 5(c)-(d), investigating pixel (8,23) shows the estimated waveform (object plus pixel bias) closely matching the true waveform while the detected waveform does not. The estimated range is 6.73 m while the true range is 6.7 m. The algorithm also implicitly estimates the pixel bias term accurately. (b) Again, using the data from Fig. 5(c)-(d), investigating pixel (16,17) shows the estimated waveform improving upon the detected waveform, but not able to match the true waveform as well as the previous pixel. The estimated range is 6.11 m while the true range is 6.7 m. Incorrect range estimation after the GEM_o algorithm relates to blurring severity (edges of cut-outs in first surface) and/or a particularly noisy realization from the Poisson distribution.

4 EXPERIMENTAL

With the simulation giving credence to the theory, experimental results are presented to fully validate the data model and the claim of improved range estimation in 3D FLASH LADAR via object recovery. Using the 3 bar target template, a laboratory experiment was conducted using 3D FLASH LADAR hardware from AFRL consistent with parameters in Table 1. As in simulation, experimental results show range estimation improvement after applying the object recovery techniques. However, several modifications to the camera and raw data were necessary to enable a proper experiment.

4.1 Spatial aliasing

Due to limits in current detector technology requiring a large footprint for the electronics behind each pixel, the receiver optics are spatially under-sampled which needs to be mitigated in order for the received data to be unaliased. This determination comes from Nyquist sampling theory in which the sampling rate must be at least twice the highest frequency content in the signal. The optics are a natural low-pass filter with the highest frequency called the cut-off frequency. For incoherent imaging, the cut-off frequency is [6]

$$f_o = \frac{D}{\lambda z_i} \quad (79)$$

where D is the aperture (exit pupil) diameter, λ is the light wavelength, and z_i is the image distance. Therefore, the focal plane must sample at twice this spatial frequency or $2D/\lambda z_i$. The typical apertures for this camera are in the centimeters. For example, an aperture of 10 cm would equate to a spatial frequency sampling requirement at 4.3×10^5 cycles per meter. At 100 μm spacing, the detector array does not meet this requirement. If the aperture is reduced to 2 mm, then the spatial frequency sampling requirement is now at 8.6×10^3 cycles per meter which the detector array can meet. However, the aperture reduction comes at the expense of reduced light gathering and shortened range in which the LADAR can be operated. Thus, the target range is placed at 5.21 meters (near the minimum ranging distance of the sensor) to obtain high enough signal to noise ratio (SNR) in the collected data.

4.2 Data pre-processing

The data observations from the 3D FLASH LADAR hardware need pre-processing steps to be suitable for insertion into the Wiener filter and GEM algorithms. In simulation, the noisy and blurry data is well-controlled and therefore, well-behaved. While the experimental 3D FLASH LADAR data exhibits expected pixel waveform shapes (i.e. Gaussian-like) and spatial blur, the data is ill-behaved to a degree due to inherent features of the hardware performance.

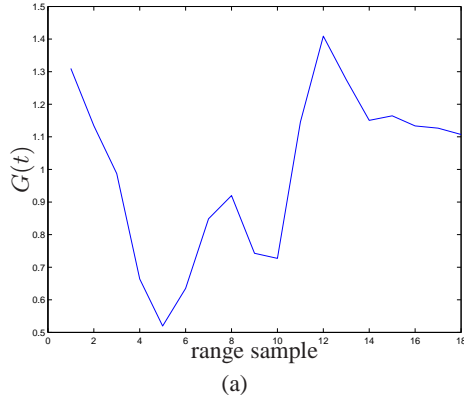
Referring to [13] and [14], the experimental hardware experiences a gain phenomenon whereby a pixel's gain drops when laser energy is incident upon a large area of another part of the detector array. With the 3 bar target, the laser energy is incident front surface first which causes second surface pixels to experience a gain drop. Figure 7(b) shows the gain drop for a second surface pixel. The method for correcting the gain is to calculate an average gain profile by looking at background pixels (i.e. returned laser energy not incident on these pixels).

Assuming the system noise follows the Poisson distribution and the gain is constant between pixels, the data model for an arbitrary pixel is

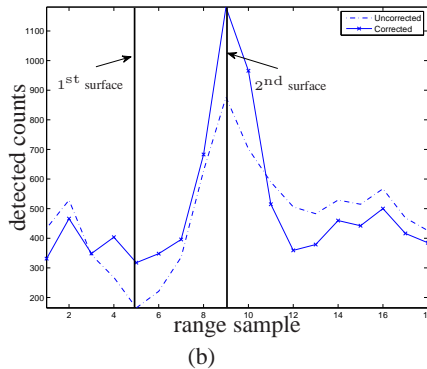
$$d(t) = G(t) [I_S(t) + I_B(t)] \quad (80)$$

where $G(t)$ is the unitless, time-varying gain, $I_S(t)$ is the laser signal in units of photons, and $I_B(t)$ is the background signal. A new variable $\hat{d}(t)$ is determined by

$$\hat{d}(t) = \frac{d(t)}{I_B(t)} \quad (81)$$



(a)



(b)

Fig. 7. (a) Gain profile correction resulting from executing Equation (84). By looking at background pixels, the hardware gain dip is clearly evident at the first surface (near range sample five) and the second surface (near range sample nine). The first surface gain drop is larger than the second surface gain drop due to the larger number of pixels illuminated (i.e. larger surface area). Amount of gain drop is proportional to received intensity level and quantity of pixels illuminated. (b) Investigating Pixel(19,32) from experimental three bar target, the pixel waveform benefits from the gain variation correction by removing the gain drop near range sample four. After correction, the pixel waveform looks more like the intended pulse model, but with unwanted noise artifacts.

where $\bar{i}_B(t) = G(t)\bar{I}_B(t)$ and is a known average background signal. It is separately calculated in the laboratory by averaging the detected background signal for selected voxels across many data cubes. Looking at the background pixels only, $\hat{d}(t)$ is

$$\hat{d}(t) = \frac{G(t)I_B(t)}{\bar{i}_B(t)} = \frac{G(t)I_B(t)}{G(t)\bar{I}_B(t)} = \frac{I_B(t)}{\bar{I}_B(t)}. \quad (82)$$

Taking the statistical variance results in

$$\begin{aligned} \text{var}(\hat{d}(t)) &= E\left[\left(\frac{I_B(t)}{\bar{I}_B(t)} - \frac{\bar{I}_B(t)}{\bar{I}_B(t)}\right)^2\right] = \frac{1}{\bar{I}_B^2(t)}E\left[(I_B(t) - \bar{I}_B(t))^2\right] \\ &= \frac{1}{\bar{I}_B^2(t)}\text{var}(I_B(t)) = \frac{\bar{I}_B(t)}{\bar{I}_B^2(t)} = \frac{1}{\bar{I}_B(t)}. \end{aligned} \quad (83)$$

Applying this result and using a sample variance of \hat{d} in place of the statistical variance ($s^2 \rightarrow \text{var}(\hat{d}(t))$), the gain is determined by

$$G(t) = \frac{\bar{i}_B(t)}{I_B(t)} = \bar{i}_B(t)s^2. \quad (84)$$

and can be seen in Fig. 7(a). This gain profile is used on each of the pixels waveforms to correct for the hardware deficiencies and to more closely match the model. For example, Fig. 7(b) shows the benefits of the gain correction for one second surface pixel. Also observed in the previous work, a side benefit of gain correction in both first and surface pixels is the waveform becomes more symmetrical. The emitted laser pulse shape is a hybrid of a Gaussian or negative parabolic shape with some asymmetry. Gain correction takes out some of the asymmetry.

The 3D FLASH LADAR is also not a photon-counting device where one digital count equals one photon. The receiver optics use Avalanche Photo Diodes (APD) where one photon equals many detected counts. Consequently, intensity scaling must be performed to condition the data to be consistent with the Poisson distribution. The conditioning is performed by using the statistics of the light and the detected mean and variance of the data. The detected mean of the data is $q\bar{K}$ where q is a scaling factor with units of photons per detected counts and \bar{K} is the true mean in units of photons. Since incoherent imaging is assumed, the detected variance becomes

$$q^2\sigma^2 = q^2\bar{K} \quad (85)$$

noting that the mean and variance of the Poisson distribution are the same. The data is scaled by solving for q and then converting the detected counts to photons by

$$d_{ph} = \frac{d_{dc}}{q} \quad (86)$$

where d_{ph} is the data in units of photons and d_{dc} is the data in units of detected counts.

4.3 Experimental PSF

The Wiener filter is used to provide a comparison to the GEM algorithm [5]. In order to implement the Wiener filter, the PSF must be known. Since the derivative of a system step response is the system impulse response, the PSF is determined by taking the derivative of a experimental step target. Figure 8(a) shows a range image of the step target collected with the same hardware as the bar target data. Although, the entire range image does not meet the requirements of being a step target due to the non-uniform intensity on the left-hand-side (LHS). Therefore, a symmetric impulse response was assumed and the right-hand-side (RHS) of the impulse response

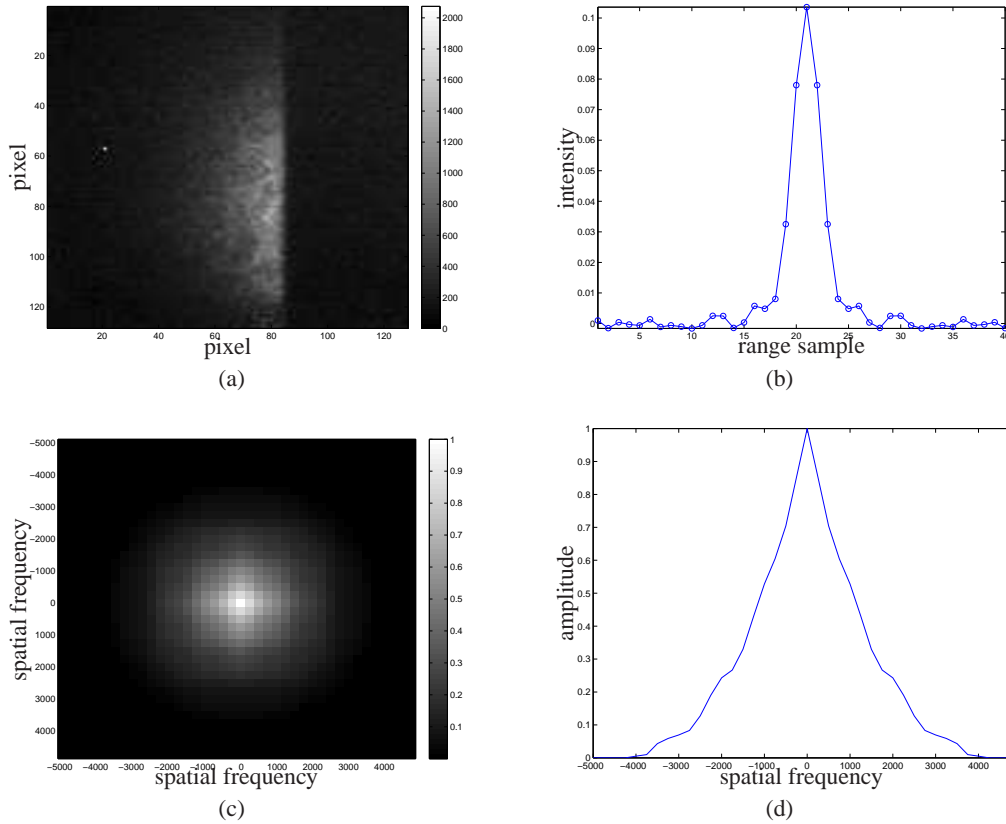


Fig. 8. (a) One range image of the step target data cube. Although the board edge is clearly visible, the variable intensity across it causes an issue with the impulse response calculation. The step response definition requires a constant amplitude at all spatial positions. The target board portion of the step response does not meet this requirement, but the non-target area (right-hand-side) does exhibit a constant amplitude. The portion of the step response function where it turns off is this non-target area. Performing the step response derivative only on this non-target area solves the problem of variable target board amplitude. (b) 1D cut-out of the resulting PSF. Assuming circular symmetry, an outer product operation is used to find the corresponding 2D PSF function. (c) Optical transfer function (OTF). The OTF is found by taking Fourier Transform of the experimental PSF [6]. (d) 1D cut-out (zero spatial frequency) of the OTF. The profile shows nearly diffraction-limited optics with a cut-off frequency at 4050 cycles per meter.

was copied and flipped over to use as the LHS. Figure 8(b) exhibits the resulting profile with an outer product operation producing the two-dimensional PSF. Phase retrieval is then performed via the Gerchberg-Saxton algorithm to arrive at the PSF used by the Wiener filter [12]. This requirement to know the PSF is a shortcoming of the Wiener filter algorithm. Figures 8(c)-(d) show the optical transfer function (OTF) where the optics exhibit a nearly diffraction-limited performance.

4.4 Results

Table 3 and Fig. 9 illustrate the range estimation benefits of object retrieval. The pulse-shape and object estimation give an RMSE improvement of 25% and 34% respectively over the original data. Additionally, the pulse-shape and object estimation give an RMSE improvement of 7% and 18% respectively over the Wiener filter algorithm. Figure 9(c) shows the image quality improvement over the original data range image in Fig. 9(b). Pixel waveforms provide additional information on the object recovery abilities. Figure 9(d) demonstrates this ability on a

Table 3. Range estimation results for experimental data

Data set	Metric	OD	WF	GEM _p	GEM _o
3 bars	RMSE	0.301	0.243	0.226	0.198
	Corr	0.818	0.883	0.900	0.924

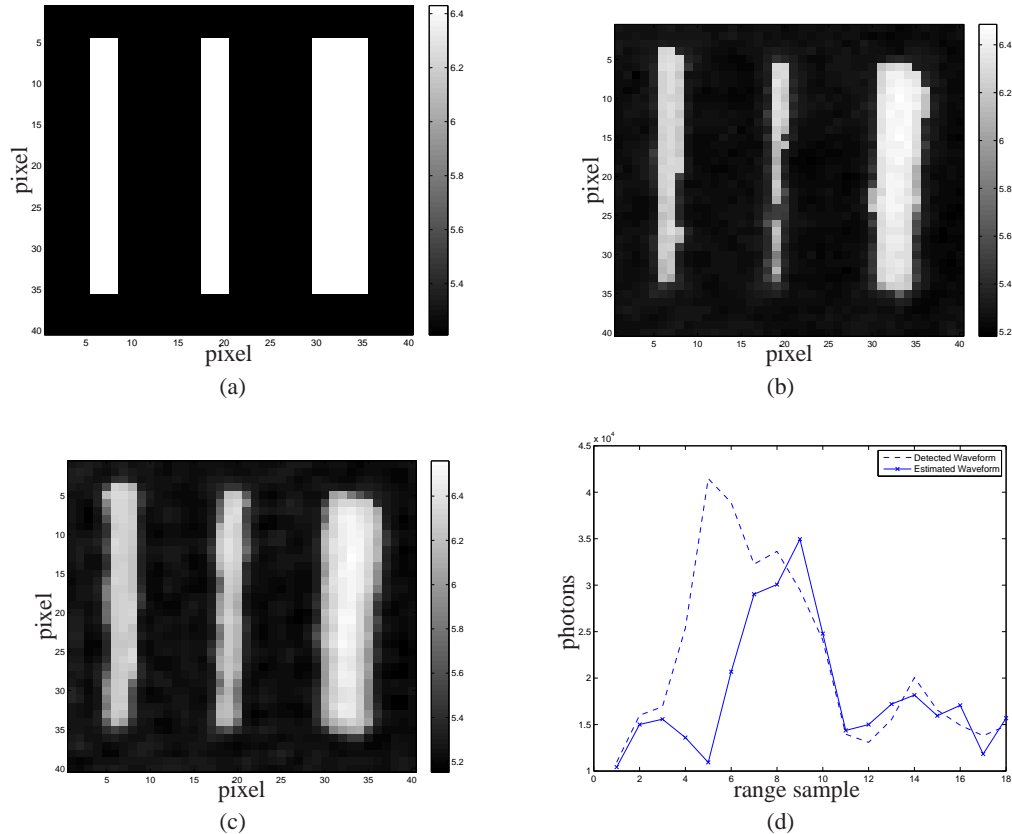


Fig. 9. Experimental target: (a) True ranges with first surface at 5.21 m and second surface at 6.43 m with 1.22 m of separation in between surfaces. (b) Ranges using normalized cross-correlation without using estimation. (c) Estimated ranges using GEM_o algorithm followed by normalized cross-correlation. (d) Considering pixel (32,18), its estimated waveform (object plus pixel bias) shows similar results from the simulated data. The estimated waveform more closely resembles the true waveform with the range close to range sample 9. Also, the algorithm correctly estimates the pixel bias confirming that the bias must arise from a noise source following the Poisson distribution (i.e. dark current).

second surface pixel, (32,18), where the raw waveform results in an incorrect range determination. In contrast, the object recovery algorithm (GEM_o) yields an improved range estimate by sufficiently estimating the true waveform.

5 CONCLUSIONS

Utilizing waveform sampling capability, the positive effects of object recovery in 3D FLASH LADAR range estimation is clearly evident. The innovative 3D FLASH LADAR sensor provides both an imaging and ranging ability enabling established theory to be applied to a novel manner. Given simulation and experimental results, it is clear the chosen model and noise sources are an appropriate choice for 3D FLASH LADAR data operating under certain conditions (SULAR mode meeting spatial sampling requirements). The raw data coming off the

sensor does not fit the model, but straight-forward pre-processing steps convert the data to an acceptable form for the algorithms.

In mild spatial blurring conditions, simulation results predict that the GEM algorithms increase range estimation performance substantially over no-processing and the Wiener filter method. Again, the Wiener filter even has an unfair advantage because it is provided with the exact PSF function used in generating the data while the GEM algorithms have to estimate the PSF. Considering the experimental data, its performance is nearly diffraction-limited as evidenced by the experimental PSF and OTF. However, the GEM algorithms still increase range estimation performance over the Wiener filter. Supported by simulation results, it is appropriate to say that the GEM algorithm would show even better range estimation performance versus the Wiener filter in severe isoplanatic atmospheric blurring conditions or with sub-optimal optics.

A trade-off exists for Wiener filter and object recovery algorithms between computation cost and range accuracy. The Wiener filter is the least computationally taxing object recovery algorithm, but is the least accurate and requires a priori knowledge of the PSF. The GEM algorithms are computationally expensive, but provides the best range performance and can perform blind deconvolution. Considering the GEM algorithms, the pulse-shape estimator is extremely valuable in that it can perform range estimation on single cube thereby removing potential for any registration or timing errors. If multiple cubes are available and properly registered, object estimation is undoubtedly the best algorithm to use. Although, none of the algorithms were able to match the success found in simulation. Any residual error in the experimental results can be attributed to system noise, the detected light containing residual laser speckle, residual gain error, and detector blurring.

There are prospective avenues for continued investigation and improvement. The pulse-shape estimation is very dependent on the selected waveform model. Improvements in the range estimation would be realized if a true waveform model for the transmitted laser pulse was derived or calculated experimentally. Errors in the experimental data result from assuming a generalized shape that is corrupted by distorting effects (spatial blur, pixel blur, and noise). In addition, the variable of interest (range term) would ideally be directly estimated. The maximum likelihood solution for the range term could be achieved if another model was discovered. The algorithm in this paper extracts the range from the maximum likelihood solution for the pulse-shape. Also, even after the pre-processing steps, the experimental data exhibits noisy behavior. A more thorough characterization of the 3D FLASH LADAR noise sources would augment or verify the chosen noise sources. Finally, isoplanatic imaging is valid for the experimental set-up in the laboratory. However, object recovery from 3D FLASH LADAR observations subject to heavy anisoplanatic turbulence would provide an ability to improve range estimation in a variety of field or operational situations.

ACKNOWLEDGEMENTS

This work was funded in part by the Air Force Office of Scientific Research (AFOSR). The authors would like to thank the Air Force Research Laboratories, Sensors Division, Wright-Patterson Air Force Base, Ohio, for the experimentally collected data used in this research. The views expressed in this paper are those of the authors and do not reflect the official policy or position of the United States Air Force, Department of Defense, or the United States Government. This document has been approved for public release; distribution unlimited.

References

- [1] J. C. Dries, B. Miles, and R. Stettner, "A 32 x 32 pixel FLASH laser radar system incorporating InGaAs PIN and APD detectors," *Proc. SPIE* **5412**, 250 (2004). [doi: 10.1117/12.542609].
- [2] R. Stettner, H. Bailey, and R. D. Richmond, "Eye-safe laser radar 3-D imaging," *Proc. SPIE* **5412**, 111 (2004). [doi: 10.1117/12.553992].

- [3] G. J. McLachlan and T. Krishnan, *The EM Algorithm and Extensions*, Wiley, Hoboken, New Jersey, 2nd ed. (2008). [doi:10.1002/9780470191613].
- [4] A. K. Jain, *Fundamentals of Digital Image Processing*, Prentice Hall, Upper Saddle River, NJ (1989).
- [5] J. McMahon, S. Cain, and R. Martin, "Improving 3-D LADAR range estimation via spatial filtering," *IEEE Aerospace Conf.*, 1–9 (2009). [doi: 10.1109/AERO.2009.4839451].
- [6] J. W. Goodman, *Introduction to Fourier Optics*, Roberts & Company, Englewood, CO (2005).
- [7] J. W. Goodman, *Statistical Optics*, McGraw-Hill, New York (1985).
- [8] S. C. Cain, R. Richmond, and E. Armstrong, "Flash light detection and ranging accuracy limits for returns from single opaque surfaces via Cramer-Rao bounds," *Appl. Optics* **45**(24), 6154–6162 (2006). [doi:10.1364/AO.45.006154].
- [9] S. Johnson and S. C. Cain, "Bound on range precision for shot-noise limited ladar systems," *Appl. Optics* **47**(28), 5147–5154 (2008). [doi:10.1364/AO.47.005147].
- [10] T. J. Schulz, "Multiframe blind deconvolution of astronomical images," *J. Opt. Soc. Am. A* **10**, 1064–1073 (1993). [doi:10.1364/JOSAA.10.001064].
- [11] L. Shepp and Y. Vardi, "Maximum-likelihood reconstruction for emission tomography," *IEEE Trans. on Medical Imag* **MI-1**(2), 113–122 (1982). [doi:10.1109/TMI.1982.4307558].
- [12] R. Gerchberg and W. Saxton, "A practical algorithm for the determination of phase from image and diffraction plane pictures," *Optik* **35**(2), 237–246 (1971).
- [13] M. D. Seal, "Nonlinear time-variant response in an avalanche photodiode array based laser detection and ranging system," Master's thesis, Air Force Institute of Technology (2007). <http://handle.dtic.mil/100.2/ADA469310>.
- [14] S. Johnson, *Range Precision of LADAR Systems*. PhD thesis, Air Force Institute of Technology (2008). <http://handle.dtic.mil/100.2/ADA488211>.

Major Jason R. McMahon received his BSEE degree in electrical engineering from the Rochester Institute of Technology in 1999 and his MSEE degree in electrical engineering from the Air Force Institute of Technology (AFIT) in 2005. He gained his Air Force commission in 1999 and worked in Atlas and Titan spacelift operations as a launch controller, launch director, instructor, and evaluator. After obtaining his masters degree, Jason worked on classified satellite programs at the National Reconnaissance Office (NRO). He is currently attending AFIT in pursuit of a PhD degree in electrical engineering.

Richard K. Martin received dual B.S. degrees (summa cum laude) in physics and electrical engineering from the University of Maryland, College Park, in 1999 and an M.S. and Ph.D. in electrical engineering from Cornell University in 2001 and 2004, respectively. He is currently an Associate Professor at the Air Force Institute of Technology (AFIT), Dayton, OH. His research interests include multicarrier equalization, blind and/or sparse adaptive filters, non-GPS navigation, source localization, image registration, and laser radar. He has authored 19 journal papers, 38 conference papers, a book chapter, and four patents. Dr. Martin was thrice elected "Instructor of the Quarter" for the Electrical and Computer Engineering Department by the AFIT Student Association, and he has twice been voted instructor of the year by the AFIT chapter of Eta Kappa Nu.

Stephen C. Cain received his BSEE degree in electrical engineering from the University of Notre Dame in 1992 and the MSEE degree in electrical engineering from Michigan Technological University in 1994. He received the PhD degree in electrical engineering from the University of Dayton in 2001. He served as an officer in the United States Air Force from 1994

to 1997. He has held the position of senior scientist at Wyle Laboratories and senior engineer at ITT Aerospace/Communications Division. He is currently an Associate Professor of electrical engineering at the Air Force Institute of Technology.